



# Computing magnetic energy and helicity fluxes from series of magnetograms

P. Démoulin and E. Pariat

Observatoire de Paris, section de Meudon, LESIA, UMR 8109 (CNRS), F-92195 Meudon Cedex, France  
e-mail: Pascal.Demoulin@obspm.fr, Etienne.Pariat@obspm.fr

**Abstract.** Magnetic energy and helicity fluxes can now be derived from measurements of the photospheric magnetic and velocity fields. We show that only photospheric flux-tube motions are needed to estimate the full fluxes. The derived maps of flux densities permit to localize where energy and helicity input occurs in active regions (ARs). The precision of the energy flux density is dominantly limited by the precision obtained on the transverse component of the magnetic field. On the contrary, the helicity flux density requires only the measurement of the vertical component of the magnetic field. Previously, the magnetic helicity maps were strongly affected by a false definition of the helicity flux density involving the magnetic vector potential. Applied to observations, this approach introduces important fake polarities. We define a better helicity flux density; it reduces the fake polarities by more than an order of magnitude. The spatial distribution of helicity injected into the studied ARs is much more coherent than previously thought, and presents a dominant sign in each AR. Finally, the correct helicity flux density could be derived from magnetograms if coronal connectivities are known.

**Key words.** magnetic fields, magnetic energy, magnetic helicity, photosphere

## 1. Introduction

The source of coronal magnetic energy and helicity lies below the surface of the sun, in the dynamo area (most likely in the tachocline). As the magnetic field gets too strong, flux tubes become buoyantly unstable, cross the convective zone (provided that they are twisted enough), emerge through the photosphere, fill the corona where they reconnect, and finally end up in the interplanetary medium, being ejected via Coronal Mass Ejections (CMEs).

The photosphere, where detailed magnetograms are presently available, is the main

source of information on the solar magnetic field. Measurements of magnetic and velocity fields can capture the fluxes of both magnetic energy and helicity crossing the photosphere. The magnetograms are a major ingredient to understand coronal phenomena such as flares and CMEs which are the main consequences of magnetic field reorganization and energy release.

An important magnetohydrodynamics (MHD) quantity is the magnetic helicity because it is well preserved, even taking into account the coronal dissipative processes (e.g. heating and reconnection). Observations of helical magnetic structures in the photosphere,

---

*Send offprint requests to:* P. Démoulin

corona and solar wind have attracted considerable attention, with a consequent interest in magnetic helicity, e.g. see reviews in Brown et al. (1999).

However, only relatively recently it has been fully realized that magnetic helicity can be derived directly from observations. Indeed, presently several groups of researchers have computed the photospheric flux of helicity: by differential rotation (DeVore, 2000; Démoulin et al., 2002; Green et al., 2002), by local horizontal motions (Chae et al., 2001; Moon et al., 2002; Nindos et al., 2003), and also by vertical motions (Kusano et al., 2002).

Below, we summarize recent advances, starting from the theoretical background (Section 2), then we review the techniques to deduce photospheric velocities (Section 3), the definition of the correct helicity flux density (Section 4), and its applications to observations (Section 5).

## 2. Definitions

Let us consider the coronal volume or a part of it,  $V$ , bounded by a closed surface,  $S$ , with a normal vector  $\hat{n}$  pointing inside  $V$ . The lower part of the surface  $S$ , called  $S_p$ , is located at the photospheric level where velocity and magnetic field observations are frequently available. On the remaining part of  $S$ , or outer part  $S_o$  ( $S = S_p + S_o$ ), no observations are available.

The magnetic energy of a field  $\mathbf{B}$  is:

$$E = \frac{1}{2\mu_0} \int_V B^2 dV. \quad (1)$$

We can define the potential field  $\mathbf{B}_p$  (without current:  $\nabla \times \mathbf{B}_p = 0$ ) which has the same normal field component at the boundary  $S_p$ :  $B_{p,n} = B_n (= \mathbf{B} \cdot \hat{n}|_{S_p})$ . Usually  $S_o$  is put at large enough distance so that  $\mathbf{B}_p$  is not significantly influenced by the boundary conditions selected on  $S_o$ .

Berger & Field (1984) have defined a relative magnetic helicity,  $H$ , subtracting the helicity of a reference field, which is classically taken as the potential field  $\mathbf{B}_p$  as defined above. An expression for  $H$ , valid for any gauge (free-

dom to add any  $\nabla f$  to  $\mathbf{A}$ ) is (Finn & Antonsen, 1985):

$$H = \int_V (\mathbf{A} + \mathbf{A}_p) \cdot (\mathbf{B} - \mathbf{B}_p) dV. \quad (2)$$

where  $\mathbf{A}$  and  $\mathbf{A}_p$  are the vector potentials of the fields  $\mathbf{B}$  and  $\mathbf{B}_p$ , respectively ( $\nabla \times \mathbf{A} = \mathbf{B}$ ,  $\nabla \times \mathbf{A}_p = \mathbf{B}_p$ ).

Let  $\mathbf{v}$  be the plasma velocity. At the photosphere, we split  $\mathbf{v}$  into tangential and normal components,  $\mathbf{v} = \mathbf{v}_t + \mathbf{v}_n$ , and the same decomposition is used for  $\mathbf{B}$  ( $= \mathbf{B}_t + \mathbf{B}_n$ ). The flux of magnetic energy through  $S_p$  satisfies

$$F_E = \frac{1}{\mu_0} \int_{S_p} [B_t^2 v_n - (\mathbf{B}_t \cdot \mathbf{v}_t) B_n] dS. \quad (3)$$

The two terms correspond to energy input in  $V$  from vertical motions (e.g. emergence of new flux) and from horizontal (e.g. shearing or twisting) motions, respectively.

The flux of the magnetic helicity through  $S_p$  is (Berger & Field, 1984):

$$F_H = 2 \int_{S_p} [(\mathbf{A}_p \cdot \mathbf{B}_t) v_n - (\mathbf{A}_p \cdot \mathbf{v}_t) B_n] dS, \quad (4)$$

where  $\mathbf{A}_p$  is computed from the distribution of  $B_n$  on  $S_p$ :

$$\mathbf{A}_p(\mathbf{x}) = \frac{\hat{n}}{2\pi} \times \int_{S_p} B_n(\mathbf{x}') \frac{\mathbf{r}}{r^2} dS' \quad (5)$$

where  $\mathbf{r} = \mathbf{x} - \mathbf{x}'$  is the vector defined by the two photospheric positions  $\mathbf{x}$  and  $\mathbf{x}'$ . The fluxes have similar formal expressions:  $F_E$  can be transformed in  $F_H$  by replacing  $\mathbf{B}_t/\mu_0$  with  $2\mathbf{A}_p$ .

## 3. Linking theory to observations

### 3.1. Available observations

The most frequently available photospheric data are the longitudinal magnetograms, the maps of the magnetic field component,  $B_{\parallel}$ , along the line of sight (e.g. MDI/SoHO). A frequently used approximation assumes that the photospheric field is vertical. This permits us to compute the normal component  $B_n$  from  $B_{\parallel}$  (obviously the closer to disk center observations are, the better the approximation).

Vector magnetographs have also been developed all around the world (e.g. THEMIS, Hinode). After calibration and removal of the  $180^\circ$  ambiguity, the  $B_{\parallel}$  and  $\mathbf{B}_{\perp}$  components can be transformed to photospheric maps of the normal,  $B_n$ , and tangential,  $\mathbf{B}_t$ , components.

Longitudinal velocities,  $v_{\parallel}$ , are classically derived from the Doppler shift of spectral lines. On the other hand, when the studied region is slightly away from the disk center, there is no safe way to transform  $v_{\parallel}$  to  $v_n$ . Thus, Doppler velocities are not used to derive energy and helicity fluxes.

One method for deriving photospheric velocities is to identify local brightness (or magnetic field) extrema and to follow them, i.e. tracking the individual magnetic features. This provides an estimation of the velocity,  $\mathbf{u}$ , of the photospheric footpoint of flux tubes (e.g., Strous et al., 1996).

A second method, more widely used, is called Local Correlation Tracking (or LCT, see Chae et al. (2001) and references therein). The velocity is locally determined by cross correlating a small fraction of two subsequent images (defined by an apodising window) shifted by a variable displacement. The relative displacement corresponds to the shift having the highest correlation; this provides an estimation of  $\mathbf{u}$ , supposing a uniform motion within the apodising window.

A third method consists in solving the vertical component of the ideal induction equation using the observed evolution of  $B_n$  (only the vertical component can be used since no reliable vertical gradient of  $\mathbf{B}$  and  $\mathbf{v}$  can be presently derived). Since only one scalar equation is available, while we have two components of  $\mathbf{u}$  to derive, the solution of the induction equation should be complemented with some input from the LCT method. Three options are presently available. A fast one, easy to implement using Fast Fourier Transform, has been proposed by Welsch et al. (2004). A more expensive one in programming and CPU time, which also require vector magnetograms, has the advantage of minimizing the input from the LCT (Kusano et al., 2002). Finally, Longcope (2004) proposed a method which uses only the

induction equation and minimizes an ad-hoc photospheric “kinetic energy” function.

Recently, Schuck (2005) developed a method to solve the induction equation in the spirit of differential LCT (solve the equation in a least square sense within the apodising window). It relaxes the global translation hypothesis of the LCT by permitting linear (affine) deformations within the apodising window. This method is called the differential affine velocity estimator (DAVE). It includes a quantitative measure of the goodness of the affine flow model. Schuck (2006) demonstrated that it outperforms the classical LCT approach on the synthetic and noisy test data. With its ability to detect flow patterns inside the apodising window, its compatibility with the induction equation and its allowance of high time cadence images (this is permitted since it is robust against noise), DAVE appears as a promising technique.

### 3.2. Estimation of photospheric fluxes

Initially, since only horizontal velocities were deduced from the temporal evolution of  $B_n$ , it was supposed that only the shear term could be derived in Equations (3,4) (e.g. Chae et al., 2001; Moon et al., 2002). However, the magnetograms of  $B_n$  permit us to follow the photospheric intersection of the magnetic flux-tubes but not the evolution of the plasma (even if the plasma is frozen in the field, the two velocities are usually different). From the observed magnetic evolution one can estimate the flux-tube motion,  $\mathbf{u}$ , not the plasma motion,  $\mathbf{v}$ , parallel to  $S_p$ , as follows. Let  $\mathbf{v}_t$  be the plasma velocity tangent to the photosphere and  $v_n$  be the velocity normal to the photosphere. The velocity of any footpoint,  $\mathbf{u}$ , is given by:

$$\mathbf{u} = \mathbf{v}_t - \frac{v_n}{B_n} \mathbf{B}_t. \quad (6)$$

Thus, Equations (3,4) simplifies to

$$F_E = -\frac{1}{\mu_0} \int_{S_p} (\mathbf{B}_t \cdot \mathbf{u}) B_n \, dS, \quad (7)$$

$$F_H = -2 \int_{S_p} (\mathbf{A}_p \cdot \mathbf{u}) B_n \, dS, \quad (8)$$

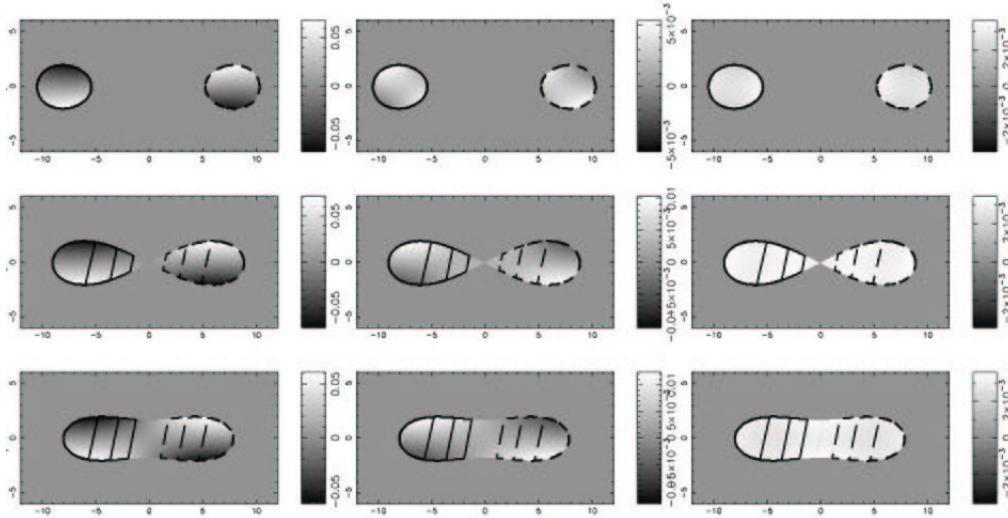


**Fig. 1.** Maps of the helicity flux density during the emergence of a weakly (0.1 turn) twisted flux tube (left:  $G_A$ , middle:  $G_\theta$ , right:  $G_\phi$ ). With  $G_A$ , the fake signals fully mask the weak positive flux. With  $G_\theta$  the fake polarities are much fainter, and it permits to detect the positive injection of helicity correctly shown by  $G_\phi$ . Notice that the values, associated to the gray levels, have changed by a factor 10 between  $G_A$  and  $G_\theta$  maps, and another factor  $\geq 2$  between  $G_\theta$  and  $G_\phi$  maps.

allowing the full energy and helicity fluxes to be deduced from temporal series of vector magnetograms (Démoulin & Berger, 2003).

## 4. Flux density of magnetic helicity

### 4.1. With the vector potential

Equation (8) seems to suggest that the quantity

$$G_A(\mathbf{x}) = -2(\mathbf{A}_p \cdot \mathbf{u})B_n \quad (9)$$

could be the helicity flux density.  $G_A$  has been used extensively to monitor the spatial distribution of magnetic helicity flux in previous studies of ARs (Chae et al., 2001; Kusano et al., 2002; Nindos et al., 2003; Moon et al., 2002).

However  $G_A$  is non null even with simple flows which do not inject any magnetic helicity to the coronal field! For example, let us consider a vertical magnetic flux tube, with  $B_n > 0$ , simply translated at a constant velocity  $\mathbf{u}$  (say,  $\mathbf{u} = U_0 \hat{\mathbf{e}}_x$ ). In the classical Coulomb gauge ( $\nabla \cdot \mathbf{A}_p = 0$ ), the vector field  $\mathbf{A}_p$  is azimuthal (like  $\mathbf{B}$  around a current wire). Thus  $G_A$  will be positive in one half ( $y > 0$ ) of

the magnetic polarity, and negative in the other half whereas no helicity should be injected!

More generally any global motions of flux tubes introduces artificial polarities of both signs in  $G_A$  maps. Another example, clearly important in solar physics, is the emergence of a flux tube. We consider a simple model to simulate the main helicity properties of this emergence. The magnetic field is confined in a torus with a main axial radius  $R_a$  and a small radius  $R$  ( $R/R_a = 0.2$  in Fig. 1). The field is uniformly twisted, both across and along the flux tube, with a number  $N$  of turns for half the torus. We simulate the emergence of half the torus with a constant vertical velocity. As shown in Fig. 1 for a weakly twisted flux tube ( $N = 0.1$ ), the maps of  $G_A$  show only negative/positive polarity pairs, just as in the above example of a translated flux tube. The globally positive helicity injection is fully masked by a fake signal.

### 4.2. With relative velocities

In order to solve the above problem,  $\mathbf{A}_p$  should be explicitly written in terms of the magnetic

field (Eq. 5). After some computations (see Pariat et al., 2005), Equation (8) is transformed to:

$$F_H = -\frac{1}{2\pi} \int_{S_p} \int_{S_p} \frac{d\theta(\mathbf{r})}{dt} B_n B'_n dS dS'. \quad (10)$$

This equation shows that the helicity injection rate can be understood as the summation of the rotation rate,  $d\theta(\mathbf{r})/dt$ , of all the pairs of elementary fluxes weighted with their magnetic flux ( $B_n dS$ ). It could then appear logical to define a helicity flux density  $G_\theta(\mathbf{x})$  as:

$$G_\theta(\mathbf{x}) = -\frac{B_n}{2\pi} \int_{S_p} \frac{d\theta(\mathbf{r})}{dt} B'_n dS'. \quad (11)$$

With a magnetic flux tube simply translated at a constant velocity,  $G_\theta = 0$  everywhere:  $G_\theta$  does not suffer the same problem as  $G_A$ . For an emerging flux tube, Figure 1 shows that  $G_\theta$  maps have still some faint fake polarities: they are apparent only in cases with a low magnetic helicity (only 0.1 turn in the example shown, this level of twist is not detectable in loop imaging). More generally, studying various examples, we show that the fake polarities in  $G_\theta$  maps are at least a factor 10 lower than the  $G_A$ 's one (Pariat et al., 2005).

#### 4.3. With coronal connectivities

While  $G_\theta$  is of great practical use, it is still not the flux density of magnetic helicity. Indeed to define it one needs the coronal connectivities of all the elementary flux tubes. The helicity flux can be rewritten as a flux of magnetic helicity per unit surface, called  $G_\Phi$  (Pariat et al., 2005).  $G_\Phi$  is a field-weighted average of  $G_\theta$  at both photospheric footpoints, located at  $\mathbf{x}_\pm$ , of the coronal connection:

$$G_\Phi(\mathbf{x}_\pm) = \frac{1}{2} \left( G_\theta(\mathbf{x}_\pm) + G_\theta(\mathbf{x}_\mp) \left| \frac{B_n(\mathbf{x}_\pm)}{B_n(\mathbf{x}_\mp)} \right| \right). \quad (12)$$

The fake signals fully disappear with  $G_\Phi$ , as illustrated in Fig. 1, the small helicity flux density is uniformly positive, as expected for the model selected.

## 5. Applications to observations

The comparison of  $G_A$  and  $G_\theta$  maps were done using the magnetic data from MDI/SoHO, the photospheric velocities being computed by local correlation tracking (Pariat et al., 2006). We showed that  $G_A$  indeed creates strong fake polarities, due to the translational motions of magnetic polarities (Sect. 4). With  $G_\theta$ , these spurious signal disappear: the non-dominant polarities of the helicity flux are suppressed and the intensities of the predominant polarities are lowered (Fig. 2).

For all the studied five ARs, the pattern of the helicity injection is much more homogeneous in  $G_\theta$  maps than in  $G_A$  maps. From the 28  $G_\theta$  maps that we studied only 3 presented intense opposite sign polarities. However for these cases, one envisions that the patterns are formed primarily by fake polarities due to  $G_\theta$ : when two oppositely signed magnetic polarities are plausibly linked (e.g. from their evolution), the real helicity flux is an average of  $G_\theta$  at these magnetic polarities (Eq. 12).  $G_\theta$  was used to remove the remnant fake polarities present with  $G_\theta$  in the case of an AR emerging nearby to another one (Pariat et al., 2006). We concluded that the spatial scale for the polarities of helicity flux density is at least of the order of the magnetic polarities if not of the scale of the whole AR.

This result has implications in three domains. First, photospheric injection is a consequence of the generation of magnetic helicity in the solar interior and of its transport in the convection zone. The cyclonic convection ( $\alpha$ -effect), which is thought to be the source of the magnetic helicity of ARs, produces simultaneously positive and negative magnetic helicity but with a spectral segregation (Ji, 1999). The observed unipolar injection of magnetic helicity would define constraints for such models.

Second, the injection of helicity with uniform sign has also implications on flare models. For example, Kusano et al. (2004) developed a mechanism based on the annihilation of opposite-sign magnetic helicity. This model was mostly based on the observations of mixed sign helicity injection. Statistical studies of the real helicity injection pattern - using  $G_\theta$  and

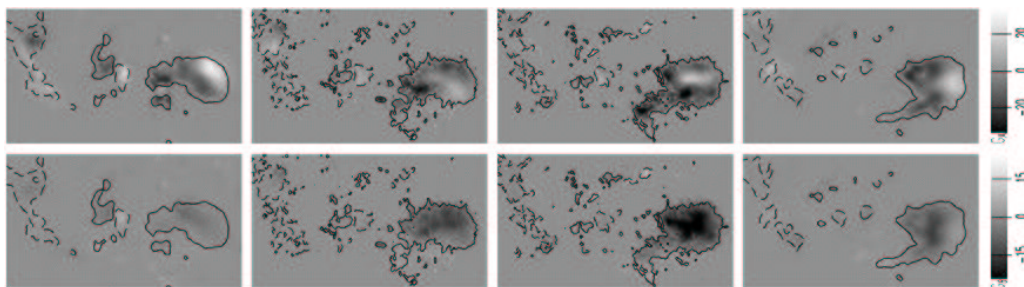


**Fig. 2.** Temporal evolution of  $G_A$  (top row) and  $G_\theta$  (bottom row) in AR 9114.  $G_A$  maps presents evolving polarities of both signs, while  $G_\theta$  maps are mostly negative. The  $G_\theta$  maps show that the total absolute helicity flux is first increasing then decreasing in magnitude (in agreement with the numerical summation of the  $G_A$  maps). The maps are in units of  $10^6 \text{ Wb}^2 \cdot \text{m}^{-2} \cdot \text{s}^{-1}$  and have  $\pm 300 \text{ G}$  isocontours of  $B_n$ .

possibly  $G_\Phi$  - linked to eruptive events must be performed to test this model (and others).

Finally, the injection of magnetic helicity with a uniform sign supports the idea that CMEs are the way for the solar atmosphere to eject helicity (which cannot accumulate forever) (Rust, 1994; Low, 1996). This can be quantitatively tested by following the injection of helicity in CME productive ARs.

In the last years, the research efforts were concentrated on magnetic helicity since its flux can be derived from longitudinal magnetograms, available with a regular cadence. With the next generation of vector magnetograms (THEMIS, Hinode, SOLIS) more precise transverse field measurements will be available. They will also permit to map the magnetic energy input. The recent progresses done in deriving photospheric flows, stimulated by the helicity research, are directly applicable to the energy flux. The complementary informations provided by vector magnetograms, maps of energy and helicity injection and magnetic extrapolations will be important tools to understand the magnetic phenomena such as flares and CMEs.

## References

- Berger, M. A. & Field, G. B. 1984, *J. Fluid. Mech.*, 147, 133
- Brown, M., Canfield, R., & Pevtsov, A. 1999, *Magnetic Helicity in Space and Laboratory Plasmas* (Geophys. Mon. Ser. 111, AGU)
- Chae, J., Wang, H., Qiu, J., et al. 2001, *ApJ*, 560, 476
- Démoulin, P. & Berger, M. A. 2003, *Sol. Phys.*, 215, 203
- Démoulin, P., Mandrini, C. H., van Driel-Gesztelyi, L., et al. 2002, *A&A*, 382, 650
- DeVore, C. R. 2000, *ApJ*, 539, 944
- Finn, J. H. & Antonsen, T. M. J. 1985, *Com. Plasma Phys. Contr. Fus.*, 9, 111
- Green, L. M., López fuentes, M. C., Mandrini, C. H., et al. 2002, *Sol. Phys.*, 208, 43
- Ji, H. 1999, *Physical Review Letters*, 83, 3198
- Kusano, K., Maeshiro, T., Yokoyama, T., & Sakurai, T. 2002, *ApJ*, 577, 501
- Kusano, K., Maeshiro, T., Yokoyama, T., & Sakurai, T. 2004, *ApJ*, 610, 537
- Longcope, D. W. 2004, *ApJ*, 612, 1181
- Low, B. C. 1996, *Sol. Phys.*, 167, 217
- Moon, Y.-J., Chae, J., Wang, H., Choe, G. S., & Park, Y. D. 2002, *ApJ*, 580, 528
- Nindos, A., Zhang, J., & Zhang, H. 2003, *ApJ*, 594, 1033
- Pariat, E., Démoulin, P., & Berger, M. A. 2005, *A&A*, 439, 1191
- Pariat, E., Nindos, A., Démoulin, P., & Berger, M. A. 2006, *A&A*, 452, 623
- Rust, D. M. 1994, *Geophys. Res. Lett.*, 21, 241
- Schuck, P. W. 2005, *ApJ*, 632, L53
- Schuck, P. W. 2006, *ApJ*, 646, 1358
- Strous, L. H., Scharmer, G., Tarbell, T. D., Title, A. M., & Zwaan, C. 1996, *A&A*, 306, 947
- Welsch, B. T., Fisher, G. H., Abbett, W. P., & Regnier, S. 2004, *ApJ*, 610, 1148